Permutation-Invariant-Polynomial Neural-Network-based Δ-Machine Learning Approach: A Case for the HO$_2$ Self-reaction and its Dynamics Study

Yang Liu and Jun Li*

School of Chemistry and Chemical Engineering & Chongqing Key Laboratory of Theoretical and Computational Chemistry, Chongqing University, Chongqing 401331, China.

AUTHOR INFORMATION

Corresponding Author

Email: jli15@cqu.edu.cn (JL)

ABSTRACT: The potential energy surface (PES) plays a central role in chemistry. As the size of the reaction system increases, it would be more and more difficult to develop its globally accurate full-dimensional PES. One unavoidable difficulty is that it is too expensive to calculate electronic energies of ample configurations for complicated reactions. Δ-machine learning, or the hierarchical construction scheme is a highly cost-effective method as only a small number of high-level *ab initio* energies are required to improve a potential energy surface (PES) fit to a large number of low-level points. Based on this idea, we propose a permutation-invariant-polynomial neural-network (PIP-NN)-based Δ-machine learning approach to construct full-dimensional accurate PESs of complicated reactions efficiently. Particularly, the high flexibility of the NN is exploited to efficiently sample points from the low-level dataset, which is very useful for the large

systems with large configuration space. The approach is applied to the $HO_2 + HO_2 \rightarrow H_2O_2 + O_2$ reaction, a key process in combustion and atmosphere. The full-dimensional triplet state PES is first constructed with a large number of density functional theory (DFT) points, which cover all dynamically relevant regions. Only 14% of the DFT dataset are used to successfully bring the DFT PES to the UCCSD(T)-F12a/AVTZ quality. On this PES of high quality, quasi-classical trajectory (QCT) calculations are performed to study the dynamics of the title reaction. A surprising mode-specific dynamics is observed, in which exciting a spectator mode leads to significant enhancement of the reactivity at low collision energy. This special mechanism can be attributed to increased attraction potential caused by the excited spectator mode. Such mode specificity may be quite prevalent in free radical reactions involving HO_2, which is common in combustion and atmosphere.

TOC GRAPHICS
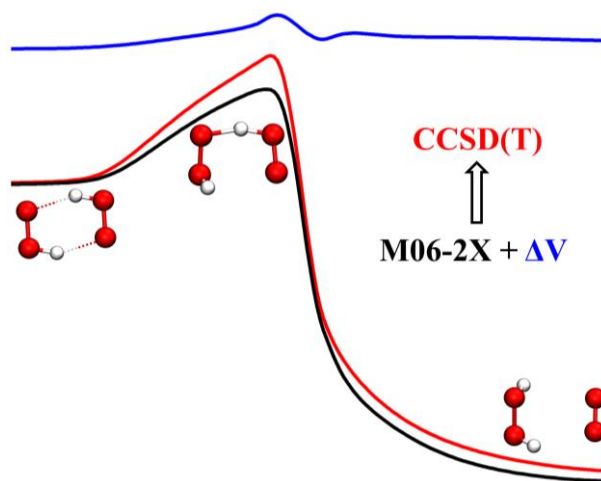
KEYWORDS   Δ-Machine Learning • Neural Network • Potential Energy Surface • Mode Specificity • Dynamics

Although several product pathways are available in the self-reaction of HO_2,[1] it is well established that the $H_2O_2 + O_2$ channel dominates on the electronic triplet state, namely,

$$HO_2 + HO_2 \rightarrow H_2O_2 + O_2 \quad \Delta H(0K) = -38.3 \pm 0.10 \text{ kcal mol}^{-1} \quad (R1).[2]$$
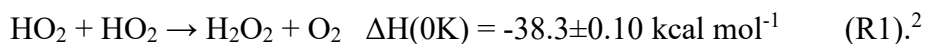
R1 is of great significance in many situations, including combustion and Earth's atmosphere. This reaction significantly affects the concentrations of HO_x radicals in the troposphere,[3] and is the main source of H_2O_2 in the atmosphere.[4-6] HO_x and H_2O_2 are widely recognized as important species in both combustion and atmosphere.[7, 8] In combustion, R1, a hydrogen abstraction reaction, is a key chain termination step that inhibits ignition. The accuracy of the kinetics for R1 is important for the performance of the combustion modeling[9] as well as engine simulations.[10]

Ample theoretical and experimental investigations have been carried out for R1 to investigate its mechanisms and kinetics over a wide range of temperatures and pressures.[4, 6, 10-24] Interestingly, it has been found that the rate coefficients of R1, denoted hereafter as k_1 (in the unit of $cm^3molecule^{-1}s^{-1}$ if not specified otherwise), show a minimum around 700-800 K. Further, the effect of pressure on k_1 is significant at low temperatures, but vanishes at temperatures above 600 K.

The aforementioned unique temperature- and pressure-dependent behaviors are related to the properties of R1 potential energy surface (PES), which governs the reaction mechanism, kinetics, and dynamics. Indeed, there exists a relatively stable intermediate between the two HO_2 radicals, namely the H_2O_4 intermediate (the HO_2 radical dimer) on the triplet state surface, whose energetics and spectroscopic characterization have also been scrutinized extensively by theory and experiment.[25-32] As shown in **Figure 1**, our calculations show that another high-energy pathway *via* $H_2OO + O_2$ leads to the same products $H_2O_2 + O_2$. To the best of our knowledge, it is the first

time that this reaction path is reported. All these features make the PES of R1 complicated. There is no PES for the title reaction, which limits our understanding for its kinetics and dynamics.

The PES, as a central role in physical chemistry, governs the nuclear dynamics that is related to molecular spectroscopy, energy transfer, chemical reactivity, and many other properties. Thanks to the advance in computing power and quantum chemistry, it is now possible to carry out *ab initio* calculations at the "gold standard" CCSD(T) (or MRCI) level for tens to hundreds of thousands of configurations for complicated systems of reasonable size. Recent years have witnessed great success in developing high-fidelity potential energy surfaces (PESs) by the machine-learning methods,[33] such as the permutationally invariant polynomial (PIP),[34] the neural network (NN),[35] or their combination PIP-NN,[36, 37] nonredundant PIP-NN,[38] and fundamental invariant (FI)-NN.[39] Thanks to the universal approximator NN, the use of the PIPs, nonredundant PIPs, or FIs as the NN input can guarantee not only the high fidelity but also the rigorous symmetry property of the molecular system with respect to the permutation of like atoms. Recent reported examples include F/Cl/H + CH_3OH,[40-42] OH +CH_4,[43] etc., for each more than 100000 UCCSD(T)-F12a/AVTZ energies were computed. The root-mean-squared error (RMSE) is generally smaller than 0.23 kcal mol^{-1} (10 meV), namely, well within the highly coveted chemical accuracy, 1 kcal mol^{-1}.
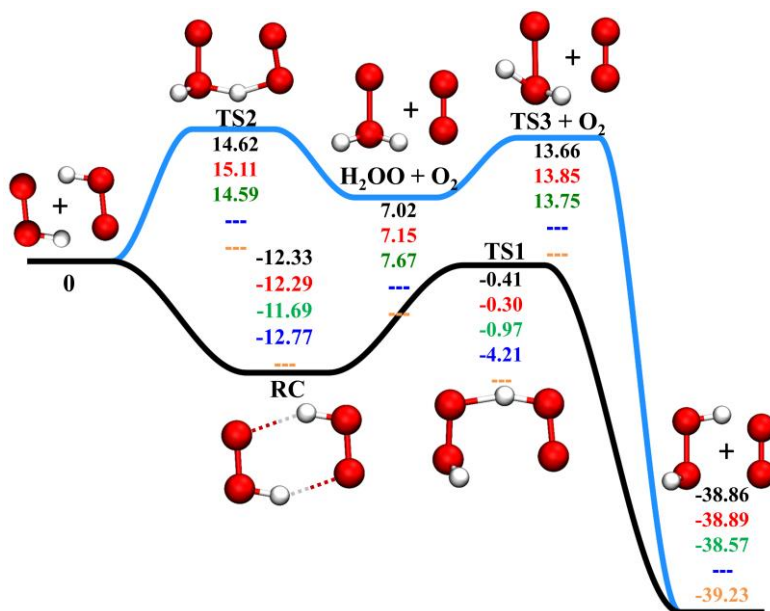
Figure 1. Schematic reaction path for the title reaction on the lowest triplet state surface. Energies are in kcal mol^{-1} and relative to the reactant asymptote: PESH, UCCSD(T)-F12a/AVTZ, UCCSD(T)-F12a/AVDZ, CASPT2/AVTZ/CBS,[44] and CCSD(T)/AVTZ/CBS,[44] from top to bottom. PESH denotes the final PIP-NN PES based on high-level energies as discussed below.

In order to develop PESs of large molecular systems accurately and efficiently, several approaches have been proposed. One promising strategy is to "correct and improve" the PES obtained at a low-level of electronic structure theory by adding the difference between low-level (LL) and some target high-level (HL) calculations. In 2008, Fu, Xu and Zhang have proposed a hierarchical construction (HC) scheme for developing accurate PESs efficiently. The target high accurate PES (V_{HL}) was expressed as a sum of a low-level PES (V_{LL}) based on dense ab initio data points and an energy difference PES (ΔV_{HL-LL}) between high- and low-level methods based on sparse data points. Namely,

$$V_{HL} = V_{LL} + \Delta V_{HL-LL}. \tag{1}$$

Thus, calculation cost can be significantly saved.[45] For the F + H_2 reaction, they sampled 15000 symmetry-unique points by a grid approach and calculated their energies by the low-accuracy UCCSD(T)/AVQZ method. Then they reduced grid density on every coordinate by roughly a factor of 2. Consequently, 1400 points were chosen from 15000 symmetry-unique points and were computed at the high-accuracy UCCSD(T)/AV5Z method. The cubic spline method was used to construct both V_{LL} and ΔV_{HL-LL}.[45] Similarly, the Δ-machine learning (ML) approach seeks to add a correction, defined as the difference between high-level and low-level calculation, to some properties (not only limited to the PES) obtained at a low-level and efficient method.[46] Transfer learning (TL) relies on the fact that knowledge gained from solving a related problem can be used to solve an unknown problem. TL is valuable to bypass the high computational cost of high-level (generally, the higher, the more accurate) electronic structure calculations. For developing PESs, a large number of low-level data (efficient to obtain) is used to first optimize a pre-trained neural network (NN), which can then be refined by a smaller number of high-level data.[47] Most TL and Δ-ML studies focused on developing general transferable force fields for thermochemistry and for molecular dynamics simulations at room temperatures or so.[46-52] In these cases, only regions around the equilibrium need be considered.

For example, Meuwly and coworkers employed the TL approach to improve a low-level MP2 NN PESs for malonaldehyde, acetoacetaldehyde, and acetylacetone (AcAc) to a high level of theory using the pair natural orbitals (PNO)-LCCSD(T)-F12 method.[47] The resulting PESs were successfully employed to reproduce finite-temperature infrared spectrum and hydrogen transfer rates. More recently, Bowman and coworkers proposed and tested a Δ-learning approach[53, 54] using PIP.[34] Specifically, they expressed the PES also as Eq. (1). However, V_{LL} denotes a PES by PIP fitting to the low-level dataset, ΔV_{HL-LL} is the correction PES also fitted by PIP fitting, and V_{HL} is

the final corrected PES of the target high quality. For CH_4, H_3O^+, and N-methylacetamide, the low-level data include DFT energies and gradients.[53] For acetylacetone, MP2 energies and gradients were used to fit V_{LL}.[54] ΔV_{HL-LL} is also a PIP fit to a much smaller database of difference between CCSD(T) and DFT or MP2 energies, as the difference PES is not sensitive as V_{LL} with respect to the change of nuclear configurations. Both efficacy and reliability of this PIP-based Δ-learning approach have been demonstrated by reproducing properties around the equilibrium of the stationary points or around the minimum energy paths (MEPs).[53, 54]

In this work, we propose a new strategy based on the idea of Δ-ML and HC. First, V_{LL}, the low-level PES, is fitted by the nonlinear PIP-neural network (PIP-NN) method.[33] Second, ΔV_{HL-LL}, the correction PES, is also learned by the PIP-NN approach.[33] Third, for each configuration, the final PES is not expressed as Eq. (1) as a sum of two functions.[45, 53, 54] In the new strategy, ΔV_{HL-LL}, based on a much smaller dataset, is employed to predict the energies of the remaining points used in V_{LL}. This is due to that ΔV_{HL-LL} spans a very small energy range and shows a "flat topography". Then for each point in the dynamically relevant configuration space, ΔV_{HL-LL} can be used to bring its potential energy to a target high level from efficient low-level calculations. Finally, these points with high-level energies are used to fit the final PES, which is again expressed as a single PIP-NN function, resulting an efficient evaluation of the PES during dynamics simulations. Essentially, this new Δ-ML approach is used to efficiently obtain the high-level energies for a large number of configurations.

The new PIP-NN based Δ-ML approach is used to develop the globally accurate full-dimensional (12D) PES of the self-reaction of HO_2 ($HO_2 + HO_2$) at the leading triplet electronic state. The PES of the bimolecular reaction $HO_2 + HO_2$ covers much wide ranges in both energy and configuration spaces. Both the asymptotic and the strongly interacting regions need be well

described as the scattering results are highly sensitive to the details of the PES, particularly for the title reaction, for which its reactant channel is complicated by the long-range interaction and its leading transition state (TS) is submerged.

Ab initio **calculations**. The reaction profile of the title reaction is illustrated in **Figure 1.** The corresponding structural parameters and harmonic frequencies of the stationary points are provided in **Figure S1** and **Table S1**, respectively. In general, the current calculations are consistent with the recent high-level theoretical results, but apparent discrepancies do exist for TS1, as discussed below.

There are two different pathways from the reactants $HO_2 + HO_2$ to the same products $H_2O_2 + O_2$. One first forms the oxywater (H_2OO) and O_2 via the transition state TS2, which is 15.11 kcal mol^{-1} higher than the reactant asymptote at the UCCSD(T)-F12a/AVTZ level. Then H_2OO, not stable, can convert to its isomer H_2O_2 easily with an isomerization barrier (TS3) of 6.64 kcal mol^{-1}. This isomerization process has been reported at various theoretical levels.[55-57] This channel (via TS2, H_2OO, TS3 to H_2O_2) has never been reported in the literature, although it is negligible due to its much high barrier even at temperatures up to 2000 K. The dominant channel is barrierless. At the UCCSD(T)-F12a/AVTZ level, a doubly hydrogen-bonded complex well (RC, -12.29 kcal mol^{-1}) is formed before reaching a hydrogen abstraction transition state (TS1, -0.30 kcal mol^{-1}). RC and TS1 have been calculated at various levels.[6, 18, 44] Here only the recent high-level results by Zhou *et al.*[44] are included for comparison. The energies of RC and TS1 were -12.77 and -4.21 kcal mol^{-1}, respectively, at CASPT2/AVTZ/CBS.[44] The characteristics of RC by Zhou *et al.*[44] were similar to the current computations. For TS1, the energy deviation between the two methods is quite large, -3.91 kcal mol^{-1}, due to the significant differences in the TS1 geometries. For example, the forming and breaking bond distances, respectively, are 1.340 and 1.088 Å at the UCCSD(T)-

F12a/AVTZ level, compared to 1.266 and 1.132 Å by Zhou *et al.*[44] In addition, as shown in **Table S1**, the imaginary frequency of TS1 is $i1884$ cm^{-1}, significantly lower in magnitude than $i2548$ cm^{-1} calculated at the level of CASPT2/AVTZ,[44] an indication of the difference in the vicinity of the PES near TS1 between the two levels. There also exists another TS (trans-like form of TS1) along R1 at other levels of theory,[6, 18, 44] but it was not successfully located at the UCCSD(T)-F12a/AVTZ level.

The reaction is highly exothermic, -38.89 (-37.79 with the zero-point vibrational energy ZPE correction) kcal mol^{-1} at the UCCSD(T)-F12a/AVTZ level. They are in line with the CASPT2/AVTZ/CBS values,[44] -39.23 (38.15) kcal mol^{-1} and the experimental value of -38.3 ± 0.10 kcal mol^{-1}.[2]

Potential energy surface. About 75300 points were calculated at the UM06-2X/AVTZ level (note that this DFT method was selected after tests, as discussed below and shown in **SI**). Their energies range from -40 to 120 kcal mol^{-1}, relative to the reactant asymptote. These points were labeled as "the entire dataset" and were fitted by the PIP-NN method. This low-level DFT PES is denoted as PESL hereafter. Then, according to the strategy described above, *ca.* 10700 points (labeled as "the training dataset") were selected from the DFT entire dataset and calculated at the UCCSD(T)-F12a/AVTZ level to develop the correction PES, ΔV_{HL-LL}. At the UCCSD(T)-F12a/AVTZ level, these 10700 points fall into the energy range from -40 to 120 kcal mol^{-1}, the same as the energy range of the DFT entire dataset. The fitted correction PES was used to bring the remaining DFT points (namely, the entire dataset without the training dataset) to the UCCSD(T)-F12a/AVTZ quality, according to Eq. (3) in **Method**. The final PIP-NN PES (denoted as PESH hereafter) is a fit to ca. 75300 high-level energies, which is composed of 10700 UCCSD(T)-F12a/AVTZ points and 64600 corrected points by the correction PES.

Figures 2*a* and **2*b*** display the distributions of the training dataset and the entire dataset, respectively, along the two reactive bond distances $R_{O'H}$ and R_{OH} up to 15 Å. The details near TS1 are shown in the insert plots. The comparison between **Figure 2a and Figure 2b** shows that 1) the two datasets have similar distributions and all key regions were well sampled; 2) the training dataset (for the correction PES) is relatively sparse and dispersed. In addition, much denser distributions around RC, TS1, and TS2 are shown in both panels and are necessary for the high-quality description around these regions.

It should be stressed that the performance of the low-level DFT method is essential. The smaller the difference between the low-level DFT and the high-level CCSD(T)-F12a, the cheaper the cost to develop the correction PES. Hence, we carried out tests on various DFT methods and the corresponding results were summarized in **Table S2**. First, the selected low-level DFT method should cover the same configuration space as the high level. Or else, the entire dataset, sampled according to the DFT level, may be not sufficient for the final PES at the target level. Second, the difference between the DFT method and the CCSD(T)-F12a should have the same trend throughout for the entire data. Or else, the correction model may be not fitted well due to the rugged differences. Further, some high-energy regions may be not readily included in common PIP-NN PESs, but are important for quantum dynamics (QD) calculations. Within the current strategy, these regions can be easily patched up by low-level computations.
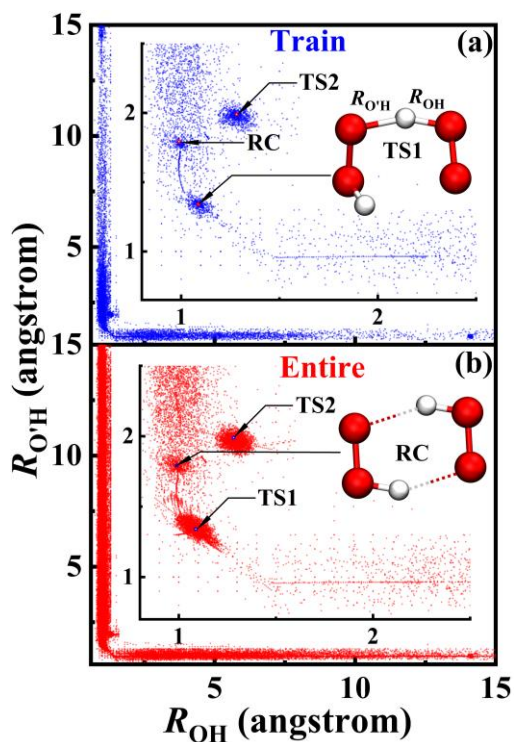
Figure 2. Distribution of the training dataset (a) and entire dataset (b) along the two reactive bond lengths up to 15 Å. The insert plots show the details near the transition state.

After a set of tests, the two hidden layers of NN were chosen to be 20 and 80, respectively, for fitting PESL, $\Delta V_{HL\text{-}LL}$, and PESH, each with 5641 fitting parameters. To minimize the random errors, the correction PES and the final PESH were chosen as the average of four and two best fittings, respectively. The RMSEs for PESL, $\Delta V_{HL\text{-}LL}$, and PESH are 0.20, 0.13, and 0.17 kcal mol^{-1}, respectively. The fitting errors of PESL are shown in **Figure S2a** as a function of the DFT energy. As seen, the fitting errors are evenly distributed in the energy up to 120 kcal mol^{-1}, and roughly 80% of the points have very low fitting errors that are less than 0.1 kcal mol^{-1}. The distribution of the DFT dataset as a function of the DFT energy is given in **Figure S2b.**

Figure S3a displays the fitting errors of $\Delta V_{HL\text{-}LL}$ as a function of the target, namely, the energy difference, UCCSD(T)-F12a minus M06-2X, HL-LL. The small fitting errors are evenly distributed along the energy range from -20 to 10 kcal mol^{-1}, which is far less than the DFT energy

range. Most errors (80%) are less than 0.1 kcal mol^{-1}, an encouraging fitting performance. **Figure S3b** presents the histogram of the 10700 training points used to build $\Delta V_{\text{HL-LL}}$. As can be seen, most absolute energy differences (85%) are less than 5 kcal mol^{-1}. A small portion of differences are larger than 10 kcal mol^{-1}. Most of these configurations are highly distorted and thus lead to large differences between UCCSD(T)-F12a/AVTZ and M06-2X/AVTZ. However, these configurations are necessary to obtain convergence of the dynamic calculations. **Figure S3c** shows the DFT energies versus the energy differences for the training points. There is no clear correlation between them. The energy range of $\Delta V_{\text{HL-LL}}$, roughly 30 kcal mol^{-1}, is much smaller than the DFT energy range of 160 kcal mol^{-1}, which ensures that only a small number of training points are needed to correct the DFT dataset, as mentioned above.

Figures S4a and S4c display the fitting errors of PESH for the training and entire dataset with respect to their corresponding high-level energies. Thanks to the ultraflexible PIP-NN approach, energies are well reproduced by the fitting for a large energy range. The distributions of the training and entire dataset as a function of the UCCSD(T)-F12/AVTZ energy are shown in **Figures S4b** and S**4d**, respectively. As seen, the two distributions have a similar shape. Most points are concentrated in the range of 0 to 30 kcal mol^{-1}.

The comparison in **Figures 2** and **S4** show that the training dataset spans nearly the same energy and configuration ranges to the entire dataset but with less dense sampling, guaranteeing that the difference PES is globally reliable. Overall, we can confidently state that the approach developed in this work can improve the PES efficiently from the low-level accuracy to the accuracy of the target high level, in this work, from UM06-2X/AVTZ to UCCSD(T)-F12a/AVTZ.

Next, we make some comments on the newly fitted PESH. As shown in **Figure S1** and **Table S1**, the energies, geometries, and harmonic frequencies of all stationary points are well reproduced

by PESL and PESH, compared with their targets, UM06-2X/AVTZ and UCCSD(T)-F12a/AVTZ, respectively. Further, to check the convergence of PESH with respect to the number of training points, 600 points were randomly selected from the QCT trajectories and then added to the training dataset after the UCCSD(T)-F12a/AVTZ calculations. The aforementioned fitting process was repeated to obtain another PES, denoted as PESH'. Then the QCT calculations were carried out on PESH and PESH' to yield reaction probabilities. As shown in **Figure 3a**, the two PESs yield almost identical reaction probabilities for the title reaction, indicating that PESH is well converged with respect to the number of training points. Indeed, these additional out-of-sample points have been well described by the PESH, as shown in **Figure 3b**. **Figure 3c** shows the target high-level energies versus energies from PESH and PESL for these 600 points. As seen, the PESH already reproduced well the target high-level energies. The deviations between target high-level energies and energies from PESH and PESL are shown in this figure. Most important, only about 14% of the DFT data points were needed to make PESH converge. For the computation time on the clusters with Intel Xeon CPU E5-2680 v3 @ 2.50 GHz processors, computing 75300 UM06-2X/AVTZ points needed about 3140 hours and the CPU time for 10700 UCCSD(T)-F12a/AVTZ points was 16050 hours. Consequently, building PESH only takes roughly 17% of CPU time for calculating 75300 UCCSD(T)-F12a/AVTZ points directly.
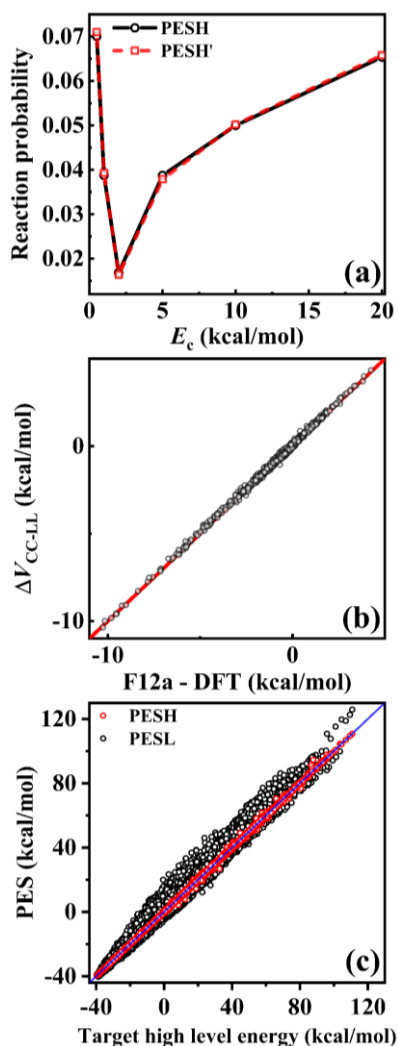
Figure 3. Testing the quality of PESH and $\Delta V_{HL\text{-}LL}$. (a) The reaction probability for the HO_2 + $HO_2 \rightarrow H_2O_2 + O_2$ reaction on PESH and PESH' (fitted with 600 more points). (b) The energy differences (in kcal mol^{-1}) from $\Delta V_{HL\text{-}LL}$ *vs* (HL - LL) ones for the 600 points randomly selected from the QCT trajectories. (c) The target high-level energies *vs* energies from PESH and PESL.

Figure 4 depicts the contour plot for the dominant reaction channel R1 on PESH as a function of the two reactive bonds $R_{O'H}$ and R_{OH} (up to 4 Å for clarity) with other degrees of freedom relaxed. RC, TS1, and PC are clearly shown. The potentials along the minimum energy path (MEP) on PESH and PESL and the corresponding energy difference between them are also shown in the inset of the same figure. As seen, PESL, PESH, and their differences are in excellent agreement

with those from the direct electronic structure calculations. With the zero of the energy as the reactant asymptote, the energy difference is quite large near the TS region along the MEP. This can be further verified in **Figure 5**, which depicts the contour of the correction PES along the two reactive coordinates. To clearly visualize the topography of PESH, the corresponding three-dimensional contour plots for R1 and the high-energy channel on the PESH are shown in **Figures S5** and **S6**, respectively.
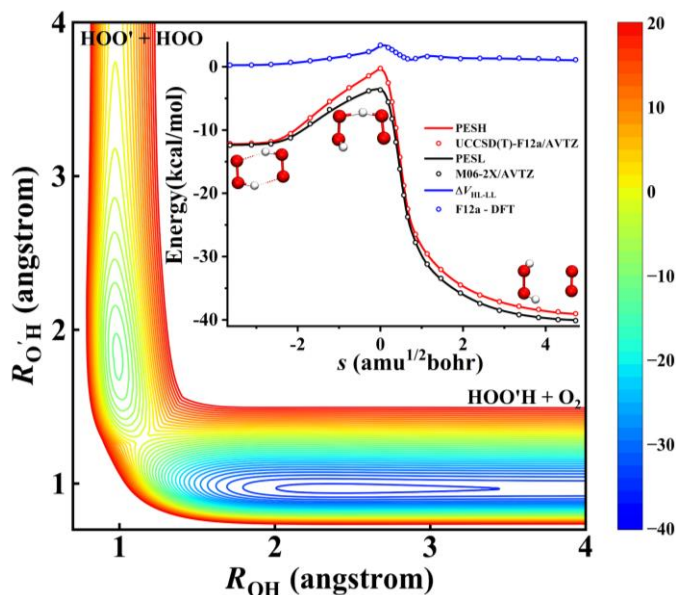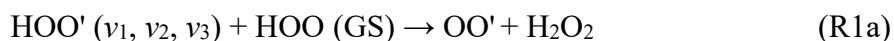

Figure 4. Contour plot for R1 on PESH as functions of the two reactive bonds $R_{O'H}$ and R_{OH} with other coordinates optimized, the energy in kcal mol^{-1}. The inset plot shows the corresponding MEPs on PESH and PESL, respectively, and determined directly by electronic structure calculations. The energy differences between UCCSD(T)-F12a/AVTZ and DFT energies and the corresponding energies on the correction PES $\Delta V_{\text{HL-LL}}$ along the MEP are also shown in the plot.
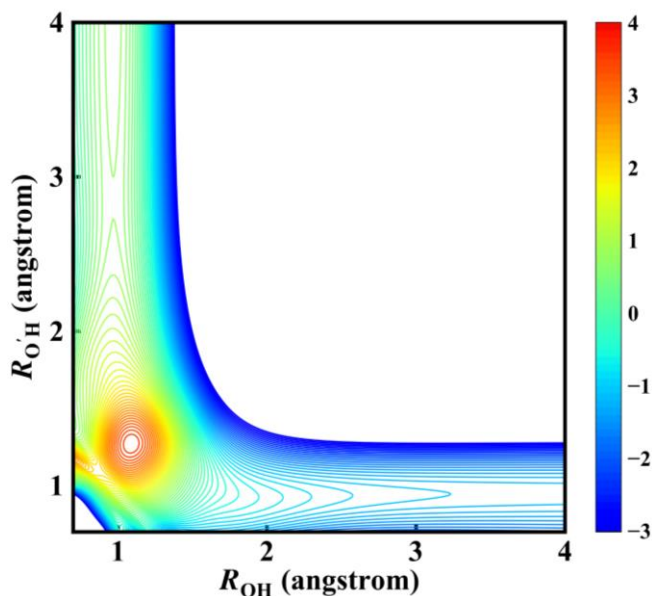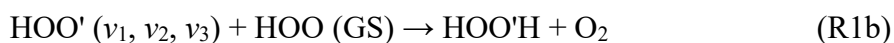
Figure 5. The contour plot of the correction PES as functions of the two reactive bonds $R_{O'H}$ and R_{OH}. The energy in kcal mol^{-1}.

Dynamics. Depositing energy in some reactant modes can enhance the reactivity, while others with additional energy have little effect on the reaction, and even inhibit the reaction. This so called mode specificity is of great importance in chemistry,[58] because it sheds light on how to control chemical processes. Thus, it has been extensively investigated in various gaseous reactions[59-63] and reactions at gas−solid interfaces.[64, 65] In the title reaction, the two same reactants HO2 can abstract hydrogen from each other. In order to conveniently explore the mode specificity of the title reaction, the reaction $HO_2 + HO_2 \rightarrow H_2O_2 + O_2$ was divided into two channels. One is

$$HOO' (v_1, v_2, v_3) + HOO \text{ (GS)} \rightarrow OO' + H_2O_2 \tag{R1a}$$

and the other is

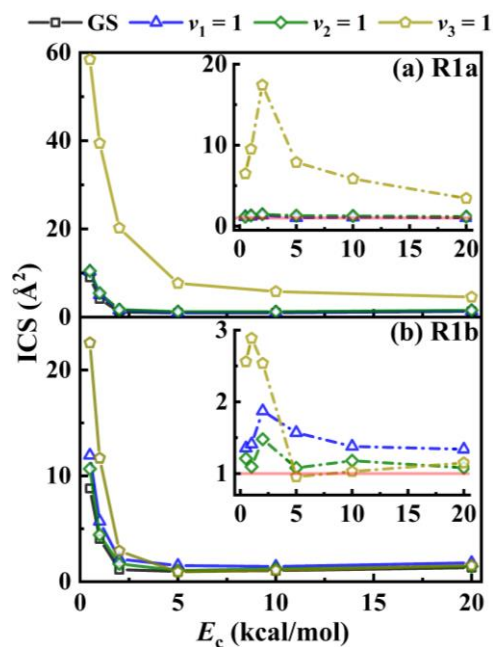$$HOO' (v_1, v_2, v_3) + HOO \text{ (GS)} \rightarrow HOO'H + O_2 \tag{R1b}$$

The initial vibrational states of one reactant HOO' are set as the ground state (GS, all $v=0$), $v_1 = 1$, $v_2 = 1$, and $v_3 = 1$, respectively, without rotational energies. v_1, v_2, and v_3 represent the vibrational quanta of OO' stretch, bending, and HO stretch motion of HO_2, respectively. The other reactant

HOO was kept at the ground vibrational state, without rotational energies. Experimentally, R1a and R1b can be distinguished by the oxygen isotopic substitution: $HO^{18}O + HOO \rightarrow O^{18}O + H_2O_2$ or $HO^{18}OH + O_2$.

Figures 6a and 6b present the QCT integral cross sections (ICSs) for R1a and R1b, respectively, with different vibrational states of HOO' as a function of collision energy E_c. The relative ICSs (defined as ICS(v)/ICS($v = 0$) are shown in the inset of **Figures 6a and 6b** for comparison. The ICS, at each state, drops sharply from 0.5 to 5.0 kcal mol^{-1} and then levels off, indicating the characteristic of the barrierless reaction. At low E_c, R1 is a complex-forming reaction and is dominated by the doubly hydrogen-bonded RC intermediate, which results in the rapid decrease of ICS. This can be also borne out by the b-weighted opacity functions of R1a and R1b, as shown in **Figures 7a** and **7b**, respectively. As seen, the accessible impact parameter b increases significantly with the decrease of E_c, confirming that the reaction is dominated by the capture of reactants at low E_c. **Figures 8a** and **8b** show the QCT differential cross sections (DCSs) of R1a and R1b at different E_c (in kcal mol^{-1}), respectively. At low E_c, the DCS is characterized with backward-forward symmetric shape, which can be attributed to the relatively long lifetime of the deep complex RC. While the backward and sideway scattering emerge with E_c, suggesting direct rebound and/or stripping mechanisms. At high E_c, the reaction is activated due to the reaction bottleneck, resulting in the slight change of ICSs with respect to E_c.

Figure 6. QCT ICSs as a function of collision energy for R1a and R1b. (a) R1a: HOO' (v_1, v_2, v_3) + HOO → OO' + H_2O_2. (b) R1b: HOO' (v_1, v_2, v_3) + HOO → HOO'H + O_2. The relative ICSs (ICS(v)/ICS($v = 0$)) are shown in the inset.
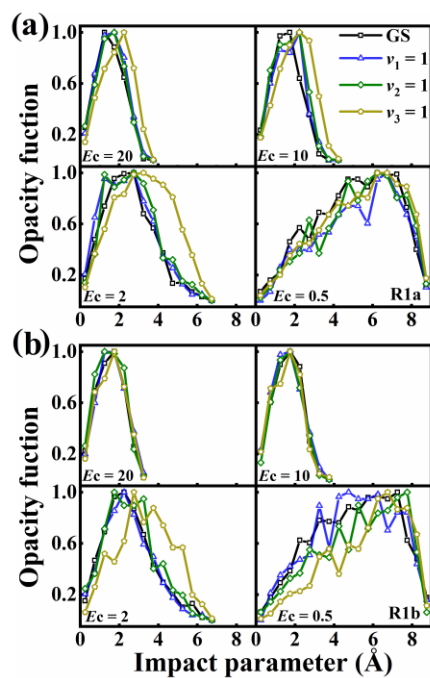

Figure 7. (a) QCT opacity functions for several initial conditions at different E_c (in kcal mol^{-1}) for R1a. (b) Similar to (a), but for R1b. The probabilities have been normalized to one.
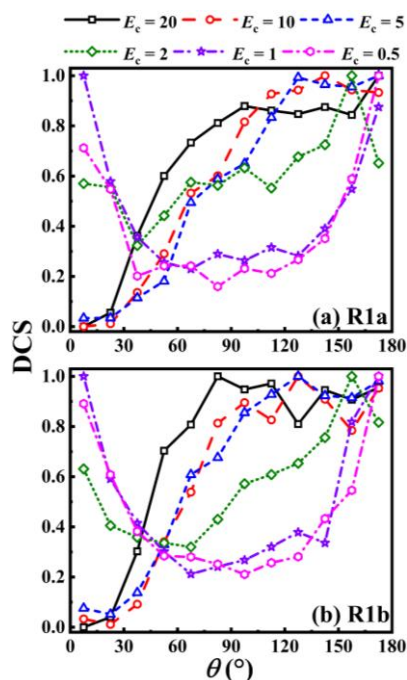
Figure 8. (*a*) QCT calculated DCSs at different E_c (in kcal mol^{-1}) for R1a. (*b*) Similar to (*a*), but for R1b. Both DCSs have been normalized to one and are for reactants being at the ground vibrational state.

Figure 9 presents the potential energies along two representative trajectories: **Figure 9a** for the direct mechanism and **Figure 9b** for the complex-forming mechanism. In the direct mechanism, the system undergoes a barrier and the product is formed via a direct hydrogen abstraction mechanism in a very short time. However, in the complex-forming mechanism, the strong attraction between reactants leads to a much longer residence time around RC than that in the direct one, particularly at low E_c. Thus, the system has enough time to adjust the relative orientation between reactants until the reaction occurs. Consequently, the reactivity is higher. In addition, one can see that the energies of PESH are in excellent agreement with the direct *ab initio* calculations for these points along the two trajectories.
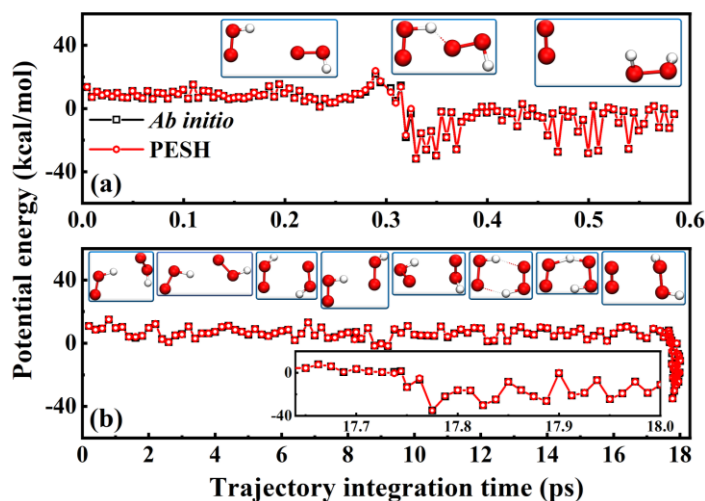
Figure 9. Direct and complex-forming mechanisms. Snapshots of representative trajectories showing the (a) direct mechanism of R1 at $E_c = 20$ kcal mol^{-1} and (b) complex-forming mechanism of R1 at $E_c = 0.5$ kcal mol^{-1}, respectively. The potential energies as a function of the QCT elapsed time were obtained from the PESH and *ab initio* calculations. Some key configurations are also shown in this figure.

Returning to the discussion of mode-specificity, as shown in **Figure 6a**, the excited HO stretch (v_3) of HOO' can significantly enhance the reactivity of R1a in the entire energy range. This is because v_3 has a strong coupling with the reaction coordinate at TS1, and depositing energy directly into the breaking bond is beneficial for the transfer of the H atom. The excitations of OO' stretch (v_1) and HOO bend (v_2) show negligible influence on the reactivity of R1a. This is not surprising. In R1a or R1b, v_1 and v_2 are both spectator modes, which are not involved in hydrogen abstraction and thus have no effects on R1a. However, a counterexample occurs in R1b. As shown in **Figure 6b**, the fundamentally excited v_3 (a spectator mode in R1b) has significant enhancement effects on the reactivity of R1b at $E_c < 5.0$ kcal mol^{-1}. Enhancing the reactivity by exciting a spectator mode was first observed in our previous work on the radical-radical reaction OH + HO$_2$ → H$_2$O + O$_2$. We attributed the special mechanism to increased dipole caused by the excited OH, which makes

the attraction between OH and HO_2 stronger.[63] Recently, Tian *et al.* reported a novel dynamical behavior that the excited low-frequency umbrella bending mode of ammonia has enhancement effects on reactivity of $F(^2P) + NH_3 \rightarrow HF + NH_2$ reaction, much more efficiently than the high-frequency stretching modes in the entire energy range of E_c, which is related to the stronger attraction induced by the excited bending mode.[66]

These unexpected results indicate that the interaction between reactants plays a significant role in the barrierless reaction, and may lead to some unique mode-specific dynamics. **Figure 10a** shows the interaction potential at different H–O (in HOO') bond distances. Clearly, the attractive interaction increases with the elongation of the H–O (in HOO') bond distance. At $R_{HO} = 1.19$ Å (corresponds to the outer turning point of $v_3 = 1$), the depth of the well is increased by roughly 3.0 and 5.6 kcal mol^{-1} relative to that at $R_{HO} = 1.08$ Å ($v_1 = 0$) and $R_{HO} = 0.97$ Å (equilibrium bond distance), respectively. The deepening of the RC well increases the chance of capturing the reactants and thus enhances the reactivity of R1b. This can be proved by **Figures 8a and 8b**, in which the long-lived RC complex results in the forward-backward symmetric DCSs at low E_c. In addition, the RC complex tends to channel the flux to TS1 due to the fact that the barrier is below the reactant asymptote. The interaction potential at different O–O' (in HOO') bond distances and HOO' bond angles are plotted in **Figures 10b** and **10c**, respectively. As seen, the depth of the well is not increased with the increase of the bond distance or angle, even slightly decreased. Hence, exciting the two modes has no significant enhancement effects on the reactivity of R1b.

Note that, the QCT approach can't consider the quantum effects, such as tunneling, zero-point energy conservation, and resonances. However, our previous quantum dynamics (QD) calculations yielded similar kinetics and dynamics results to the QCT calculated ones for a similar radical-radical reaction OH + $HO_2 \rightarrow H_2O + O_2$.[63, 67]
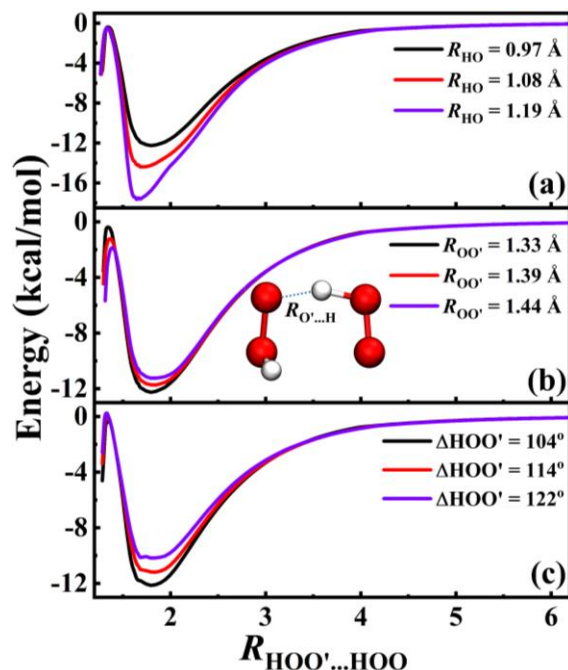
Figure 10. Intramolecular geometry-dependent interaction potentials. (a) Interaction potential between the two reactants as a function of O'H (O' in HOO' and H in HOO) distance with other degrees of freedom relaxed for several H–O bond lengths of HOO'. The H–O bond lengths of 0.9719, 1.0847, and 1.1921 Å are corresponding to the equilibrium bond distance , $v_3 = 0$, and $v_3 = 1$, respectively. (b) Similar to (a), but for O–O' bond lengths of HOO'. (c) Similar to (a), but for angle HOO'.

In summary, the performance of any PES reaches at most the same level of accuracy as the underlying reference data. Various density functional theory (DFT) methods have found wide successful and efficient applications for chemistry, physics, and materials related fields. However, the DFT accuracy can't be guaranteed generally, particularly for molecular systems.[68] Thus, accurate theories, such as the "gold standard" CCSD(T) or MRCI with a large basis set, are necessary. Unfortunately, it is still prohibitive to determine energies of a large data set for complicated systems. Further, our tests have shown that for the title reaction, CCSD(T) method

22

may easily run into convergence issues or predict a wrong-state energy, particularly for regions of multireference nature, as found also in another important reaction in combustion and atmosphere, $OH + HO_2 \rightarrow H_2O + O_2$.[69] The newly proposed Δ-machine learning approach is efficient to obtain high-level energies for a large number of points.

Indeed, the newly proposed approach is, to some extent, similar to the composite approach proposed and developed by Pople and other pioneering theorists. The chemical accuracy can be efficiently reached at the computationally cost of combinations of these models.[51] Briefly, the target high-level energy can be obtained by adding various corrections, which were crafted to determine efficiently,

$$E_{\mathrm{HL}} = E_{\mathrm{LL}} + \Delta E_{\mathrm{IL_1-LL}} + \Delta E_{\mathrm{IL_2-IL_1}} + \cdots + \Delta E_{\mathrm{HL-IL}_i} \tag{2}$$

with LL for low level, IL$_i$ for the intermediate level i, and HL for target high level. Given an appropriate low-level calculation, the problem then becomes how to determine accurate and efficient estimation for ΔEs. Consequently, one can determine the energies for a large number of configurations efficiently within the hierarchy scheme.[45] Further, one can improve previous PESs by adding more and more corrections gradually,[45] which is invaluable for the science community of developing PESs and related fields.

However, how to efficiently sample points from the low-level dataset is a key issue, as the computational cost is directly determined by the sampling size. Therefore, we propose in this work an NN-based Δ-machine learning approach for developing full-dimensional accurate PES. Taking advantage of the uncertainty of the NN potentials, we can efficiently select points from the low-level dataset. To test the effectiveness of this approach, we construct the first accurate full-dimensional ground triplet state PES for the $HO_2 + HO_2 \rightarrow H_2O_2 + O_2$ reaction. Finally, only about 14% (10700) of the DFT data points (75300) are used to accurately bring the DFT PES of this

system to UCCSD(T)-F12a/AVTZ level. This newly fitted PIP-NN based Δ-machine learning approach will be used to build PESs of larger systems in our future work. Note, other NN approaches can be also used to replace PIP-NN to train the correction PES.

Based on the newly fitted PES, the QCT calculations are carried out to study the dynamics of the title reaction. We find a special mode-specificity dynamics, namely, exciting the spectator HO stretch mode of HOO' can significantly enhance the reactivity of the title reaction at low collision energy, which was first reported in our previous work of the OH + HO$_2$ → H$_2$O + O$_2$ reaction.[63] Unlike the conventional mode specificity, this special mechanism can be attributed to increased attraction potential caused by the excited OH. As pointed out earlier by us, such special mode specificity effect may be prevalent in combustion and atmospheric reactions.[63] More interesting dynamics will be expected in various complicated reactions once their full-dimensional accurate PESs are developed, for instance, by the present efficient approach.

PIP-NN based Δ-ML method. For the PES of the title system, the first step is to construct a low-level DFT PES at the selected UM06-2X/AVTZ level. Developing PESs of reactive systems has been detailed in our previous work,[33, 70] and thus is not repeated here. Overall, the PES was gradually improved until all relevant dynamical results were converged and key properties, including geometries, frequencies, and energies of the stationary points, were well reproduced, compared to the direct UM06-2X/AVTZ calculations. In addition, some points were selected by the grid approach, which may sample configurations of high energy. These points are necessary for future quantum dynamical calculations, although these points may be not relevant by QCT.

The next step is building a correction PES to correct the UM06-2X/AVTZ dataset. Specifically, the UM06-2X/AVTZ dataset was partitioned into two parts. One small subset was the training dataset, whose energies were re-calculated at the level of UCCSD(T)-F12a/AVTZ. Then the

differences between UCCSD(T)-F12a/AVTZ and M06-2X/AVTZ energies for this small subset were used to train the correction PES ΔV_{HL-LL}. This correction PES can be used to predict the energy differences of the remaining points of the UM06-2X/AVTZ dataset for the low-level PES. Namely, their energies were not calculated by the direct and expensive UCCSD(T)-F12a/AVTZ calculations, but were corrected according to the following equation:

$$E_{HL} = E_{LL} + \Delta E_{HL-LL}, \tag{3}$$

where E_{LL} is the DFT energy, ΔE_{HL-LL} is the correction part predicted by ΔV_{HL-LL}, and ΔE_{HL} is the final energy of the high-level accuracy. Then the final PES of the title system was refitted to the high-level dataset. Clearly, our strategy is different from Bowman and co-workers' approach[53, 54] in which the final Δ-learning PIP PES was described as the sum of the DFT PES and correction PES ΔV_{HL-LL}. For the subset used to train the correction PES, its error might be enlarged by fitting twice, in comparison to our strategy, in which for the subset used to train the correction PES ΔV_{HL-LL}, their UCCSD(T)-F12a/AVTZ energies were directly employed in the final fitting. Further, the present approach is free of the additional evaluation cost of the correction PES in the dynamic calculations, as the correction PES is only used to predict the energy difference between low- and high-level computations.

It's crucial to sample configurations efficiently from the DFT dataset, as the computational cost is directly determined by the sampling size. In the HC scheme, the grid approach was used to sample points from the low-level dataset. This method is efficient for the tri-atom $F + H_2$ system, but is unfeasible for larger systems due to the exponential growth of the number of data points with the system size. Bowman and co-workers used root mean square (RMS) bond difference between two configurations as the criterion to select points near the equilibrium of stationary points and chose a random integer that indicated their position on a list of the remaining points to

select points in other regions, which produced a subset that spans the same range of configurations as the original DFT dataset.[54] A small number of configurations were needed to reproduce the key properties around the equilibrium of the stationary points or along the MEP.[53, 54] However, this sampling method is prohibitively expensive for the title reaction with a large configuration space and it's desirable to sample points efficiently to make the correction PES $\Delta V_{\text{HL-LL}}$ converged with fewer high-level energies.

It's well known that the NN-based potentials are represented by nonlinear "non-physical" functions and have limited extrapolation capabilities. Therefore, in principle, if some regions were not covered well, namely, lacking points, different NN potentials would have large uncertainty for configurations of these regions. Based on this fact, Behler and co-workers exploited the high flexibility of the NN to search the poorly sampled regions of the configuration space.[71] Namely, if some points possess large energy deviations between two NN fits, they were added to the training set. Recently, Lin *et al*. proposed a trajectory-free active learning method,[72] based on this idea, to iteratively add new data points for sampling. It has been demonstrated that an accurate PES can be developed with much fewer points than the trajectory-based methods.

In this work, we also utilize the limited extrapolation capabilities of NN potential to select points from the DFT dataset. First, 1500 points were chosen from the DFT dataset and then calculated to obtain their electronic energies at the UCCSD(T)-F12a/AVTZ level. For these 1500 points, 500 geometries were selected near the equilibrium of the stationary points, and another 1000 were well dispersed along the MEP from reactants to products. Note that a larger Euclidean distance

$\chi(\{r_i\}) = \sqrt{\sum_i^{15} |\vec{r_i} - \vec{r_i'}|^2}$ defined in terms of the internuclear distances between two points, $\{\vec{r_i}\}$ and $\{\vec{r_i'}\}$,

in the data set was used in this step than that used in the development of the DFT PES because only a smaller number of points were needed for the construction of the corrections PES.

Then the PIP-NN fitting was carried out to obtain the preliminary correction PES. To minimize the random error of NN fit, according to the NN ensemble approach, four best NN fittings were chosen to calculate the average energy difference among them, namely,

$$D = \frac{\sum_{i<j}^{4} \left| \Delta V_{\text{HL-LL}}^{i} - \Delta V_{\text{HL-LL}}^{j} \right|}{6}, \tag{4}$$

where $\Delta V_{\text{HL-LL}}^{i}$ and $\Delta V_{\text{HL-LL}}^{j}$ are the ith and jth correction PES, respectively. The energy differences of each remaining point in the DFT dataset were calculated. Then the first 300 points with the biggest energy deviations were added to the training dataset for the correction PES. Note that the generalized Euclidean distance was again used to exclude points that are close to each other. The procedure mentioned above was iterated to gradually improve the correction PES until the final PES can provide converged dynamical results and reproduce the key properties, such as geometries, frequencies, and energies of all stationary points, compared to the target high-level UCCSD(T)-F12a/AVTZ calculation.

ASSOCIATED CONTENT

Supporting Information

The Supporting Information is available free of charge on the ACS Publications website at DOI. Details of electronic structure calculations, PIP-NN fitting, and quasi-classical trajectory (QCT) calculations are given in the Supplementary Information, SI.

AUTHOR INFORMATION

Corresponding Author

Jun Li − School of Chemistry and Chemical Engineering & Chongqing Key Laboratory of Theoretical and Computational Chemistry, Chongqing University, Chongqing 401331, China; orcid.org/0000-0003-2392-8322; Email: jli15@cqu.edu.cn

Notes

The authors declare no competing financial interests.

REFERENCES

(1) Sahetchian, K. A.; Heiss, A.; Rigny, R. Formation of molecular hydrogen by thermal decomposition of n-dialkyl peroxides in oxygen. *J. Phys. Chem.* **1987**, *91*, 2382-2386.

(2) Ruscic, B.; Pinzon, R. E.; Morton, M. L.; Srinivasan, N. K.; Su, M.-C.; Sutherland, J. W.; Michael, J. V. Active thermochemical tables: Accurate enthalpy of formation of hydroperoxyl radical, HO_2. *J. Phys. Chem. A* **2006**, *110*, 6592-6601.

(3) Stone, D.; Rowley, D. M. Kinetics of the gas phase HO_2 self-reaction: Effects of temperature, pressure, water and methanol vapours. *Phys. Chem. Chem. Phys.* **2005**, *7* (10), 2156-2163.

(4) Stockwell, W. R. On the $HO_2 + HO_2$ reaction: Its misapplication in atmospheric chemistry models. *J. Geophys. Res-Atmos.* **1995**, *100*, 11695-11698.

(5) Lesko, T. M.; Colussi, A. J.; Hoffmann, M. R. Hydrogen isotope effects and mechanism of aqueous ozone and peroxone decompositions. *J. Am. Chem. Soc.* **2004**, *126*, 4432-4436.

(6) Anglada, J. M.; Olivella, S.; Sole, A. New insight into the gas-phase bimolecular self-reaction of the HOO radical. *J. Phys. Chem. A* **2007**, *111*, 1695-1704.

(7) Tyndall, G. S.; Cox, R. A.; Granier, C.; Lesclaux, R.; Moortgat, G. K.; Pilling, M. J.; Ravishankara, A. R.; Wallington, T. J. Atmospheric chemistry of small organic peroxy radicals. *J. Geophys. Res-Atmos.* **2001**, *106*, 12157-12182.

(8) Hansen, A. S.; Bhagde, T.; Moore, K. B.; Moberg, D. R.; Jasper, A. W.; Georgievskii, Y.; Vansco, M. F.; Klippenstein, S. J.; Lester, M. I. Watching a hydroperoxyalkyl radical (•QOOH) dissociate. *Science* **2021**, *373*, 679-682.

(9) Seal, P.; Papajak, E.; Truhlar, D. G. Kinetics of the hydrogen abstraction from carbon-3 of 1-butanol by hydroperoxyl radical: Multi-structural variational transition-state calculations of a reaction with 262 conformations of the transition state. *J. Phys. Chem.. Lett.* **2012**, *3*, 264-271.

(10) Som, S.; Liu, W.; Zhou, D. D. Y.; Magnotti, G. M.; Sivaramakrishnan, R.; Longman, D. E.; Skodje, R. T.; Davis, M. J. Quantum tunneling affects engine performance. *J. Phys. Chem. Lett.* **2013**, *4*, 2021-2025.

(11) Lii, R.-R.; Gorse, R. A.; Sauer, M. C.; Gordon, S. Temperature dependence of the gas-phase self-reaction of hydroperoxo radicals in the presence of ammonia. *J. Phys. Chem.* **1980**, *84*, 813-817.

(12) Niki, H.; Maker, P. D.; Savage, C. M.; Breitenbach, L. P. An FTIR study of the mechanism for the gas phase reaction between HO_2 radicals. *Chem. Phys. Lett.* **1980**, *73*, 43-46.

(13) Patrick, R.; Pilling, M. J. The Temperature-dependence of the HO_2 + HO_2 reaction. *Chem. Phys. Lett..* **1982**, *91*, 343-347.

(14) Takacs, G. A.; Howard, C. J. Temperature dependence of the reaction hydroperoxo (HO_2) + hydroperoxo at low pressures. *J. Phys. Chem.* **1986**, *90*, 687-690.

(15) Atkinson, R.; Baulch, D. L.; Cox, R. A.; Hampson, R. F.; Kerr, J. A.; Troe, J. Evaluated kinetic and photochemical data for atmospheric chemistry: Supplement III. IUPAC subcommittee on gas kinetic data evaluation for atmospheric chemistry. *J. Phys. Chem. Ref. Data* **1989**, *18*, 881-1097.

(16) Lightfoot, P. D.; Veyret, B.; Lesclaux, R. The rate constant for the $HO_2 + HO_2$ reaction at elevated temperatures. *Chem. Phys. Lett.* **1988**, *150* (1-2), 120-126.

(17) Hippler, H.; Troe, J.; Willner, J. Shock wave study of the reaction $HO_2 + HO_2 \rightarrow H_2O_2 + O_2$: Confirmation of a rate constant minimum near 700 K. *J. Chem. Phys.* **1990**, *93*, 1755-1760.

(18) Zhu, R. S.; Lin, M. C. The self-reaction of hydroperoxyl radicals: ab initio characterization of dimer structures and reaction mechanisms. *Physchemcomm* **2001**, 4, 1-6.

(19) Christensen, L. E.; Okumura, M.; Sander, S. P.; Salawitch, R. J.; Toon, G. C.; Sen, B.; Blavier, J. F.; Jucks, K. W. Kinetics of $HO_2+HO_2 \rightarrow H_2O_2+O_2$: Implications for stratospheric H_2O_2. *Geophys. Res. Lett.* **2002**, *29*, 1229.

(20) Donaldson, D. J.; Francisco, J. S. Bimolecular reaction of molecular oxygen with overtone excited HOOH: Implications for recycling HO2 in the atmosphere. *Phys. Chem. Chem. Phys.* **2003**, *5*, 3183-3187.

(21) Hong, Z.; Davidson, D. F.; Hanson, R. K. An improved H_2/O_2 mechanism based on recent shock tube/laser absorption measurements. *Combust. Flame* **2011**, *158*, 633-644.

(22) Hong, Z.; Lam, K.-Y.; Sur, R.; Wang, S.; Davidson, D. F.; Hanson, R. K. On the rate constants of $OH + HO_2$ and $HO_2 + HO_2$: A comprehensive study of H_2O_2 thermal decomposition using multi-species laser absorption. *Proceed. Combust. Inst.* **2013**, *34*, 565-571.

(23) Zhang, T. L.; Bi, X. J.; Wen, M. J.; Liu, S.; Chai, G.; Zeng, Z. P.; Wanga, R.; Wang, W. L.; Long, B. The $HO_4H \rightarrow O_3 + H_2O$ reaction catalysed by acidic, neutral and basic catalysts in the troposphere. *Mol. Phys.* **2020**, *118*, 1-11.

(24) Assali, M.; Rakovsky, J.; Votava, O.; Fittschen, C. Experimental determination of the rate constants of the reactions of $HO_2 + DO_2$ and $DO_2 + DO_2$. *Int. J. Chem. Kinet.* **2020**, *52*, 197-206.

(25) Diem, M.; Tso, T. L.; Lee, E. K. C. On the bonding and structure in dihydroperoxyl $(HO_2)_2$ and H_2O_4. *J. Chem. Phys.* **1982**, *76*, 6452-6454.

(26) Fitzgerald, G.; Schaefer, H. F. The cyclic, two-hydrogen bond from of the HO_2 dimer. *J. Chem. Phys.* **1984**, *81*, 362-367.

(27) Fitzgerald, G.; Lee, T. J.; Schaefer, H. F.; Bartlett, R. J. The open chain or chemically bonded structure of H_2O_4: The hydroperoxyl radical dimer. *J. Chem. Phys.* **1985**, *83*, 6275-6282.

(28) Fermann, J. T.; Hoffman, B. C.; Tschumper, G. S.; Schaefer, H. F. The hydroperoxyl radical dimer: Triplet ring or singlet string? *J. Chem. Phys.* **1997**, *106*, 5102-5108.

(29) Hollman, D. S.; III, H. F. S. In search of the next Holy Grail of polyoxide chemistry: Explicitly correlated *ab initio* full quartic force fields for HOOH, HOOOH, HOOOOH, and their isotopologues. **2012**, *136*, 084302.

(30) Sprague, M. K.; Irikura, K. K. Thermochemistry of $HO_2 + HO_2 \rightarrow H_2O_4$: Does HO_2 dimerization affect laboratory studies? *J. Phys. Chem. A* **2015**, *119*, 7052-7062.

(31) Kim, H.-D.; Seo, H.-I.; Song, H.-S.; Kim, S.-J. Theoretical investigation of the structures and spectroscopic properties of $(H_2O_4)n$ ($n = 1–4$) clusters. *Int. J. Quantum Chem.* **2016**, *116*, 1427-1436.

(32) Martins-Costa, M. T. C.; Anglada, J. M.; Ruiz-Lopez, M. F. Structure of hydrogen tetroxide in gas phase and in aqueous environments: relationship to the hydroperoxyl radical self-reaction. *Struct. Chem.* **2016**, *27*, 231-242.

(33) Jiang, B.; Li, J.; Guo, H. High-fidelity potential energy surfaces for gas-phase and gas–surface scattering processes from machine learning. *J. Phys. Chem. Lett.* **2020**, *11*, 5120-5131.

(34) Qu, C.; Yu, Q.; Bowman, J. M. Permutationally invariant potential energy surfaces. *Annu. Rev. Phys. Chem.* **2018**, *69*, 151-175.

(35) Chen, J.; Xu, X.; Xu, X.; Zhang, D. H. Communication: An accurate global potential energy surface for the $OH + CO \rightarrow H + CO_2$ reaction using neural networks. *J. Chem. Phys.* **2013**, *138*, 221104.

(36) Jiang, B.; Guo, H. Permutation invariant polynomial neural network approach to fitting potential energy surfaces. *J. Chem. Phys.* **2013**, *139*, 054112.

(37) Li, J.; Jiang, B.; Guo, H. Permutation invariant polynomial neural network approach to fitting potential energy surfaces. II. Four-atom systems. *J. Chem. Phys.* **2013**, *139*, 204103.

(38) Lu, D.; Li, J. Full-dimensional global potential energy surfaces describing abstraction and exchange for the $H + H_2S$ reaction. *J. Chem. Phys.* **2016**, *145*, 014303.

(39) Shao, K.; Chen, J.; Zhao, Z.; Zhang, D. H. Communication: Fitting potential energy surfaces with fundamental invariant neural network. *J. Chem. Phys.* **2016**, *145*, 071101.

(40) Weichman, M. L.; Devine, J. A.; Babin, M. C.; Li, J.; Guo, L.; Ma, J.; Guo, H.; Neumark, D. M. Feshbach resonances in the exit channel of the $F + CH_3OH \rightarrow HF + CH_3O$ reaction observed using transition-state spectroscopy. *Nat. Chem.* **2017**, *9*, 950-955.

(41) Lu, D.; Li, J.; Guo, H. Comprehensive Investigations of the Cl + CH_3OH → HCl + CH_3O/CH_2OH reaction: Validation of experiment and dynamic insights. *CCS Chem.* **2020**, *2*, 882–894.

(42) Lu, D.; Behler, J.; Li, J. Accurate global potential energy surfaces for the H + CH_3OH reaction by neural network fitting with permutation invariance. *J. Phys. Chem. A* **2020**, *124*, 5737-5745.

(43) Li, J.; Guo, H. Communication: An accurate full 15 dimensional permutationally invariant potential energy surface for the OH + CH_4 → H_2O + CH_3 reaction. *J. Chem. Phys.* **2015**, *143*, 221103.

(44) Zhou, D. D. Y.; Han, K.; Zhang, P.; Harding, L. B.; Davis, M. J.; Skodje, R. T. Theoretical determination of the rate coefficient for the HO_2 + HO_2 → H_2O_2+O_2 reaction: Adiabatic Treatment of anharmonic torsional effects. *J. Phys. Chem. A* **2012**, *116*, 2089-2100.

(45) Fu, B.; Xu, X.; Zhang, D. H. A hierarchical construction scheme for accurate potential energy surface generation: An application to the F + H_2 reaction. *J. Chem. Phys.* **2008**, *129*, 011103.

(46) Ramakrishnan, R.; Dral, P. O.; Rupp, M.; von Lilienfeld, O. A. Big Data Meets Quantum chemistry approximations: The delta-machine learning approach. *J. Chem. Theory Comput.* **2015**, *11*, 2087-2096.

(47) Käser, S.; Unke, O. T.; Meuwly, M. Reactive dynamics and spectroscopy of hydrogen transfer from neural network-based reactive potential energy surfaces. *New J. Phys.* **2020**, *22*, 055002.

(48) Chmiela, S.; Sauceda, H. E.; Müller, K.-R.; Tkatchenko, A. Towards exact molecular dynamics simulations with machine-learned force fields. *Nat. Commun.* **2018**, *9*, 3887.

(49) Smith, J. S.; Nebgen, B. T.; Zubatyuk, R.; Lubbers, N.; Devereux, C.; Barros, K.; Tretiak, S.; Isayev, O.; Roitberg, A. E. Approaching coupled cluster accuracy with a general-purpose neural network potential through transfer learning. *Nat. Commun.* **2019**, *10*, 2903.

(50) Sauceda, H. E.; Chmiela, S.; Poltavsky, I.; Müller, K.-R.; Tkatchenko, A. Molecular force fields with gradient-domain machine learning: Construction and application to dynamics of small molecules with coupled cluster forces. *J. Chem. Phys.* **2019**, *150*, 114102.

(51) Zaspel, P.; Huang, B.; Harbrecht, H.; von Lilienfeld, O. A. Boosting Quantum machine learning models with a multilevel combination technique: Pople diagrams revisited. *J. Chem. Theory Comput.* **2019**, *15*, 1546-1559.

(52) Stöhr, M.; Medrano Sandonas, L.; Tkatchenko, A. Accurate many-body repulsive potentials for density-functional tight binding from deep tensor neural networks. *J. Phys. Chem. Lett.* **2020**, *11*, 6835-6843.

(53) Nandi, A.; Qu, C.; Houston, P. L.; Conte, R.; Bowman, J. M. Delta-machine learning for potential energy surfaces: A PIP approach to bring a DFT-based PES to CCSD(T) level of theory. *J. Chem. Phys.* **2021**, *154*, 051102.

(54) Qu, C.; Houston, P. L.; Conte, R.; Nandi, A.; Bowman, J. M. Breaking the coupled cluster barrier for machine-learned potentials of large molecules: The case of 15-Atom acetylacetone. *J. Phys. Chem. Lett.* **2021**, *12*, 4902-4909.

(55) Meredith, C.; Hamilton, T. P.; Schaefer, H. F. Oxywater (water oxide): New evidence for the existence of a structural isomer of hydrogen peroxide. *J. Phys. Chem.* **1992**, *96*, 9250-9254.

(56) Huang, H. H.; Xie, Y.; Schaefer, H. F. Can Oxywater Be Made? *J. Phys. Chem.* **1996**, *100*, 6076-6080.

(57) Sayos, R.; Oliva, C.; Gonzalez, M. A theoretical approach to the $O(^1D)+H_2O(X^1A_1)$ reaction: *Ab initio* potential energy surface and quasiclassical trajectory dynamics study. *J. Chem. Phys.* **2000**, *113*, 6736-6747.

(58) Polanyi, J. C. Some concepts in reaction dynamics. *Science* **1987**, *236*, 680-690.

(59) Crim, F. F. Vibrational state control of bimolecular reactions: Discovering and directing the chemistry. *Acc. Chem. Res.* **1999**, *32*, 877-884.

(60) Crim, F. F. Bond-selected chemistry: vibrational state control of photodissociation and bimolecular reaction. *J. Phys. Chem.* **1996**, *100*, 12725-12734.

(61) Li, J.; Jiang, B.; Guo, H. Reactant vibrational excitations are more effective than translational energy in promoting an early-barrier reaction $F + H_2O \rightarrow HF + OH$. *J. Am. Chem. Soc.* **2013**, *135*, 982-985.

(62) Liu, K. Vibrational Control of Bimolecular Reactions with Methane by Mode, Bond, and Stereo Selectivity. *Annu. Rev. Phys. Chem.* **2016**, *67*, 91-111.

(63) Liu, Y.; Song, H.; Xie, D.; Li, J.; Guo, H. Mode specificity in the $OH + HO_2 \rightarrow H_2O + O_2$ reaction: Enhancement of reactivity by exciting a spectator Mode. *J. Am. Chem. Soc.* **2020**, *142* (7), 3331-3335.

(64) Juurlink, L. B. F.; Killelea, D. R.; Utz, A. L. State-resolve probes of methane dissociation dynamics. *Prog. Surf. Sci.* **2009**, *84*, 69-134.

(65) Chadwick, H.; Beck, R. D. Quantum state–resolved studies of chemisorption reactions. *Annu. Rev. Phys. Chem.* **2017**, *68*, 39-61.

(66) Tian, L.; Song, H.; Yang, M. Effects of bending excitation on the reaction dynamics of fluorine atoms with ammonia. *Phys. Chem. Chem. Phys.* **2021**, *23*, 2715-2722.

(67) Liu, Y.; Song, H.; Li, J. Kinetic study of the $OH + HO_2 \rightarrow H_2O + O_2$ reaction using ring polymer molecular dynamics and quantum dynamics. *Phys. Chem. Chem. Phys.* **2020**, *22* (41), 23657-23664.

(68) Li, G.; Zhou, L.; Li, Q.-S.; Xie, Y.; Schaefer III, H. F. The entrance complex, transition sate, and exit complex for the F + H$_2$O → HF + OH reaction. Definitive predictions. Comparison with popular density functional methods. *Phys. Chem. Chem. Phys.* **2012**, *14*, 10891-10895.

(69) Liu, Y.; Bai, M.; Song, H.; Xie, D.; Li, J. Anomalous kinetics of the reaction between OH and HO2 on an accurate triplet state potential energy surface. *Phys. Chem. Chem. Phys.* **2019**, *21*, 12667-12675.

(70) Jiang, B.; Li, J.; Guo, H. Potential energy surfaces from high fidelity fitting of *ab initio* points: The permutationinvariant polynomial neural network approach. *Int. Rev. Phys. Chem.* **2016**, *35*, 479.

(71) Behler, J. Neural network potential-energy surfaces in chemistry: a tool for large-scale simulations. *Phys. Chem. Chem. Phys.* **2011**, *13*, 17930-17955.

(72) Lin, Q.; Zhang, Y.; Zhao, B.; Jiang, B. Automatically growing global reactive neural network potential energy surfaces: A trajectory-free active learning strategy. *J. Chem. Phys.* **2020**, *152*, 154104.